Kubo conductivity tensor for two- and three-dimensional magnetic nulls

D. A. St-Onge* and R. D. Sydora†
Department of Physics, University of Alberta, Edmonton, Alberta, Canada T6G 2E1
(Received 4 February 2014; published 2 September 2014)

The complete Kubo conductivity tensor is computed in two- and three-dimensional linear magnetic null systems using collisionless single-particle simulations. Regions of chaotic charged-particle dynamics are constructed for each case. It is found that stochastic frequency mixing of particle bounce motion, as well as gyromotion, contribute significantly to the conductivity. The conductivity curves are well approximated by power laws over a certain frequency range and the ac conductivity is found to be an order of magnitude smaller than the dc value, leading to enhanced resistivity, particularly near the cyclotron frequency. The ac conductivities must be accounted for in computation of the total dissipation.

DOI: 10.1103/PhysRevE.90.033103 PACS number(s): 52.20.Dq, 52.25.Gj, 05.45.−a, 52.65.Cc

I. INTRODUCTION

Magnetic reconnection is the process in which magnetic field lines from two or more distinct fields cross-connect and reassemble themselves in a plasma to form new magnetic configurations. This is driven by the release of stored magnetic energy through dissipative processes such as classical collisions or anomalous resistivity. The consequence of reconnecting magnetic fields is the possible formation of a magnetic null (alternatively, a magnetic neutral point), which is the area between distinct magnetic domains, providing the magnitude of the field becomes zero.

Giovanelli [1] suggested that an electric field near a magnetic null point has the ability to accelerate free electrons, leading to a possible mechanism for solar flares. Neutral points were soon applied to models of the magnetosphere by Hoyle [2]. Dungey [3] developed the theory of magnetic reconnection and its relation to magnetic neutral points. Electric fields near null points can heat and accelerate particles towards areas of stronger magnetic field, resulting in energy being carried away from the magnetic field which drives magnetic reconnection; this has been demonstrated in recent laboratory experiments, e.g., Ref. [4]. The time scale of an average solar flare is on the order of 10^2–10^3 s. To explain this rapid or explosive magnetic energy release, a fast reconnection mechanism was formulated by Petschek [5] and has been generalized by others [6,7]. While this mechanism yields correct time scales, previous magnetohydrodynamics simulations have failed to reproduce these results when applied to nulls with homogeneous resistivity [8]. Recently, Baty *et al.* have been able to reproduce correct time scales using Petschek reconnection with homogeneous resistivity but with nonuniform viscosity profiles [9]. One of the main difficulties in magnetic reconnection calculations is establishing the dominant temporal and length scales of the process. While collisional reconnection processes can be modeled fairly well using uniform resistivities, systems with nonuniform resistivity and three-dimensional effects are less understood. Also, the theory behind collisionless reconnection is not very well developed.

One important aspect of magnetic reconnection is the conductivity (or resistivity) around the region of reconnecting field lines, where the magnitude of the conductivity can determine the time scale of the process by calculating the dissipation $D = \int_V \mathbf{E}\cdot\mathbf{j}\,dx$, where $\mathbf{E}$ is the electric field, $\mathbf{j}$ is the current, and V is over the entire space and time domain of the dissipation region. To determine $\mathbf{E}$, Ohm's law can be used for low-β magnetic fields, $\mathbf{j} = \sigma\mathbf{E}$, where σ is the conductivity tensor. There is no exact method of calculating the conductivity tensor, therefore different methods must be studied and compared.

Speiser showed that resistivity can exist without particle collisions or wave interactions [10]. He derived two collisionless resistivities, one based on the gyromotion of particles and another based on nonadiabatic acceleration around regions of magnetic diffusion. Another method for calculating the conductivity is the Kubo formalism [11,12]. One advantage of the Kubo conductivity is its ability to compute conductivities over an entire spectrum of applied electric fields. Similar to the Kubo conductivity is the linearized Vlasov conductivity, which is derived by using a kinetic theory of plasmas. For ergodic systems, the Kubo conductivity and linearized Vlasov conductivity are equivalent [12]. Previous work on fluctuating electric fields and electromagnetic disturbances in the vicinity of magnetic field nulls have focused on energy redistribution time scales and particle acceleration processes [13–16]. In this work we consider the ac conductivity due to stochastic frequency mixing of gyromotion and particle bounce motion.

Martin [17] studied the chaotic dynamics of the two-dimensional X point using the method of Lyapunov exponents for a variety of situations. It was found that even without an applied electric field, dynamics around a null point are generally chaotic. Numata and Yoshida [18,19] calculated the conductivity of an expanded X point (known as a double-Y point) by using a conductivity similar to that derived by Speiser and calculated the reconnection dynamics by using Petschek's model. It was found that a single chaos zone, while enhancing the resistivity of the system, cannot solely account for fast-type reconnection.

In a series of papers Horton *et al.* investigated the collisionless DC conductivity in a two-dimensional approximation to the magnetic null in the geomagnetic tail by using the

*Current address: Princeton Plasma Physics Laboratory, Princeton, New Jersey, United States P. O. Box 451, 08543-0451; dstonge@pppl.gov
†rsydora@ualberta.ca

Vlasov conductivity [12,20,21]. It was found that stochastic processes near the magnetic null resulted in power-law decays of the correlation of velocities with an effective collision time, proportional to the cyclotron period, being used to calculate the energy dissipation of the system. Holland and Chen [22] criticized the use of the Vlasov conductivity in a number of ways, stating that it may not satisfy the necessary conditions needed to render it valid near magnetic null points. It was also found that the Vlasov conductivity was sensitive to the total integration time of the simulation. For long simulation times, particles would also spend most of their time in nonchaotic regions, rendering a definition of conductivity based on chaotic motion ambiguous. Afterwards, they proposed a method to find the energy dissipation of particles based on a method by Cowley [23], which is derived from the difference of ingoing and outgoing particle pitch angles. Finally, they note that their results contradict results found by Speiser [10], stating that the simple relation $\mathbf{j} = \sigma \mathbf{E}$ may not be valid in plasmas. Hernandez and Horton presented calculations demonstrating that long-term correlated motion near regions of chaos lead to important contributions to the conductivity, as well as arguing that the necessary conditions are met in order to apply the Vlasov conductivity [24].

In recent years, more attention has been given to the reconnection near three-dimensional null points. These null points offer a large variety of different topological configurations. Cowley [25] first studied the structure of a three-dimensional potential null of the form $\mathbf{B} = (\alpha x, \beta y, -(\alpha + \beta)z)$, stating that the neutral point consisted of a spine with field lines expanding to a so-called fan plane. Fukao *et al.* [26] studied more general neutral points, finding spiral structures. He noted that, in general, the spine and the fan of the null are not perpendicular. Parnell *et al.* performed a complete study on all possible types of three-dimensional linear nulls, as well as degenerate two-dimensional null cases [27]. Recently, the European Space Agency Cluster satellites observed a three-dimensional magnetic null in the Earth's magnetosphere [28]. The four separated spacecraft enabled a detailed analysis of the field structure and indicated a spatial scale on the order of the ion inertial length (c/ω_{pi}).

The purpose of this study is to construct the complete frequency-dependent conductivity tensor of the potential null points described in Parnell's study [27] by using the Kubo conductivity formula, as well as to gain insight into the validity of the equivalent Vlasov conductivity used by Horton *et al.* In this paper the ac conductivity of the double-Y point in Numata and Yoshida [18] has been computed using the Kubo formalism and compared with the mean-drift method [18] which only yields the dc value. Lyapunov exponents for all systems are determined to better understand the underlying chaotic dynamics. Finally, the energy dissipation has been computed and compared to regular dynamics further away from magnetic null points.

This paper is organized as follows: Section II describes the procedure used in computing Lyapunov exponents and the conductivities of interest, as well as the methodology of the computer simulations. Section III deals with the study of the two-dimensional system from Numata and Yoshida [18], as well as the comparison of the Kubo and Speiser conductivities. Section IV contains the study of the three-dimensional potential null systems outlined in Parnell *et al.* [27]. The discussion of the results as well as the summary are presented in Sec. V.

II. SIMULATION APPROACH

The simulation of microscopic particle dynamics in the vicinity of magnetic nulls is based on a system of noninteracting particles in an electromagnetic field with the equations of motion

$$m\frac{d\mathbf{v}}{dt} = q[\mathbf{E}(\mathbf{x}) + \mathbf{v} \times \mathbf{B}(\mathbf{x})], \tag{1}$$

where q and m are the charge and mass of the particle, respectively. In this simulation normalized units are used where $\hat{\mathbf{x}} = \mathbf{x}/L$, $\hat{\mathbf{b}} = \mathbf{B}/B_0$, $\hat{t} = t/\tau_A$, $\hat{\mathbf{v}} = \mathbf{v}/v_A$, $\hat{\mathbf{e}} = \mathbf{E}/m_A v_A B_0$, where $v_A = B_0/\sqrt{\mu_0 n m}$ is the Alfvén velocity, n is the plasma density, B_0 is the magnitude of the magnetic field, $\tau_A \equiv L/v_A$, L is the scale-length of the experiment, and $m_A = E_0/B_0 v_A$ is the Alfvén Mach number. The magnetic field in the Alfvén velocity is taken as the asymptotic unit magnetic field. This gives a normalized equation of motion,

$$\frac{\lambda_i}{L}\frac{d\hat{\mathbf{v}}}{d\hat{t}} = m_A\hat{\mathbf{e}} + \hat{\mathbf{v}} \times \hat{\mathbf{b}},$$

where $\lambda_i = c/\omega_p$. Here c is the speed of light and ω_p is the plasma frequency for the specified particle species. We let $L = \lambda_i$ so $\tau_A^{-1} = \omega_c$. Although the results from this study can be scaled for both electrons and ions, it is assumed that since the ion Larmor radius is much greater than that of the electron, most effects will be the result from ion motion, as it will experience greater chaotic effects by being closer to the magnetic null. The equations of motion are integrated explicitly with particle positions being evaluated at every integer step and the particle velocities, as well as the electromagnetic fields, being evaluated at every half-integer step. All simulations are run with a time step of $\Delta\hat{t} = 0.01$ so cyclotron motion is accurately resolved. Particle velocities are initialized using a Maxwellian distribution with $\hat{v}_T = v_T/v_A = 0.05$.

Initial particle positions are uniformly distributed over the region of chaos around the magnetic neutral point. This region of chaos is determined by the growth rate of the unnormalized maximal Lyapunov exponent (uMLE), which is the maximal Lyapunov exponent λ_1 [29,30] multiplied by the time step, i.e.,

$$\lambda_1 t = \ln\frac{\sqrt{\Delta\mathbf{r}(t)\cdot\Delta\mathbf{r}(t)}}{\sqrt{\Delta\mathbf{r}_0\cdot\Delta\mathbf{r}_0}}, \tag{2}$$

where t is the time of the simulation, $\Delta\mathbf{r}$ is the difference between the phase-space vectors of two trajectories which are infinitesimally separated at $t = 0$, and the dot product$(\cdot)$ denotes the inner product in a six-dimensional phase space. When particles are close to the magnetic null, the uMLE grows linearly, while particles far away from the null experience weak growth. The region of chaos is determined by plotting points along a particle trajectory where the time derivative of $\lambda_1 t$ is greater than a specified threshold value, which is unity for these simulations. In practice, 100 particles are used in the simulations lasting 100 000 time steps to determine the chaos region.

The $\mu\nu$ component of the conductivity tensor is computed using the Kubo conductivity formula [11]

$$\sigma_{\mu\nu}(\omega) = \frac{nq^2}{mv_T^2}\int_0^\infty e^{-i\omega t}\langle v_\nu(0)v_\mu(t)\rangle dt, \tag{3}$$

where ω is the frequency of the perturbation electric field, v_T is the initial thermal velocity, and $\langle\dots\rangle$ denotes the ensemble average. The Kubo conductivity is derived by using the fluctuation-dissipation theorem [31] in a magnetic system. The integrand of the Kubo conductivity deals with velocities of the unperturbed equilibrium magnetic field, so in all of our simulations, $\mathbf{E} = 0$. When the system is ergodic, the ensemble average can be replaced with a time-average, giving

$$\sigma_{\mu\nu}(\omega) = \frac{nq^2}{mv_T^2}\frac{1}{N}\sum_N\int_0^\infty \lim_{T\to\infty}\frac{1}{T} \times \int_0^T e^{-i\omega\tau}v_\nu(t)v_\mu(t+\tau)dtd\tau, \tag{4}$$

where the conductivity is averaged over N particles. This is equivalent to the conductivity tensor derived from the Vlasov equation. In normalized units this becomes

$$\hat{\sigma}_{\mu\nu}(\hat{\omega}) = \frac{1}{N\hat{v}_T^2}\sum_N\int_0^\infty \lim_{\hat{T}\to\infty}\frac{1}{\hat{T}} \times \int_0^{\hat{T}} e^{-i\hat{\omega}\hat{\tau}}\hat{v}_\nu(\hat{t})\hat{v}_\mu(\hat{t}+\hat{\tau})d\hat{t}d\hat{\tau}. \tag{5}$$

The systems considered in this paper were determined to be ergodic by computing both Eqs. (3) and (4). This is explained in detail for the two- and three-dimensional cases in Secs. III and IV, respectively.

A useful theorem to note here is the cross-correlation theorem,

$$\int_{-\infty}^\infty \bar{A}(t)B(t+\tau)dt = \frac{1}{2\pi}\int_{-\infty}^\infty \bar{A}(\omega)B(\omega)e^{-i\omega t}d\omega, \tag{6}$$

which states that the correlation of variables A and B is simply the inverse Fourier transform of the power spectrum between variables A and B, where the overbar signifies the complex conjugate. When $A = B$, this theorem reduces to the Wiener-Khinchin theorem. Therefore, it follows that the Vlasov conductivity is simply proportional to the power spectrum of velocity v_μ and v_ν. As a corollary, when the Vlasov conductivity is integrated over all frequencies,

$$\int_0^\infty d\omega \mathrm{Re}\,\sigma(\omega) = \frac{nq^2}{m}\frac{\pi}{2}, \tag{7}$$

which can be seen by taking the inverse Fourier transform of the power spectrum with $t = 0$.

Numata and Yoshida [18] derived a dc conductivity ($\omega = 0$) based on the dissipative equation in normalized form,

$$\hat{\rho}\frac{d\hat{\bar{v}}}{d\hat{t}} = m_A\hat{e}_z - \hat{\nu}_{\mathrm{eff}}\hat{\bar{v}}, \tag{8}$$

with the following analytical solution for the mean-drift ($\hat{\bar{v}}$):

$$\hat{\bar{v}} = \frac{m_A\hat{e}_z}{\hat{\nu}_{\mathrm{eff}}}\left[1 - \exp\left(-\frac{\hat{\nu}_{\mathrm{eff}}}{\hat{\rho}}\hat{t}\right)\right]. \tag{9}$$

Here $\hat{\rho}$ is the effective test particle mass (normalized by the ion mass), $\hat{\nu}_{\mathrm{eff}}$ is an effective collision frequency, and $\hat{e}_z$ is the z component of the normalized electric field. Using Ohm's law, we define an effective resistivity η_{eff},

$$E_z = \eta_{\mathrm{eff}}j_z = \eta_{\mathrm{eff}}nq\bar{v}_{\mathrm{sat}}, \tag{10}$$

where n is the density and $\bar{v}_{\mathrm{sat}}$ is defined as the asymptotic limit of the average z velocity for large times given by $\hat{\bar{v}}_{\mathrm{sat}} = m_A\hat{e}_z/\hat{\nu}_{\mathrm{eff}}$ in normalized form. From this, one can show that the resistivity is

$$\frac{\eta_{\mathrm{eff}}}{\mu_0} = \lambda_i^2\omega_c\hat{\nu}_{\mathrm{eff}}, \tag{11}$$

where $\lambda_i = c/\omega_{pi}$ is the ion skin depth and ω_{pi} the ion plasma frequency. The conductivity is simply the reciprocal of the resistivity. This Kubo conductivity can also be expressed as an effective collision time through

$$\hat{\nu}_{\mathrm{eff}}^{-1} = \sigma_{zz}(0)\mu_0\lambda_i^2\omega_{ci} = \frac{1}{N\hat{v}_T^2}\sum_{i=1}^N\int_0^\infty \lim_{\hat{T}\to\infty}\frac{1}{\hat{T}}\int_0^{\hat{T}}\hat{v}_z(\hat{t})\hat{v}_z(\hat{t}-\hat{\tau})d\hat{t}d\hat{\tau}. \tag{12}$$

It is important to note that the mean-drift method gives an enhanced local conductivity near the region of chaotic motion. Furthermore, the collision time based on this method and the Vlasov (or Kubo) conductivity may greatly differ, as will be discussed later.

III. 2D MAGNETIC NULL CONDUCTIVITY

Before applying the Kubo conductivity to the three-dimensional magnetic null, we construct the conductivity tensor for a previously studied two-dimensional null. Numata and Yoshida [18] proposed an extension to the two-dimensional X-type null using the magnetic field model

$$\mathbf{B} = \begin{cases}[B_0(y \mp l_y)/l_x, B_0x/l_x, 0] & (\pm y > l_y),\\ (0, B_0x/l_x, 0) & (|y| \leqslant l_y),\end{cases} \tag{13}$$

where $l_x = l_y = 1$ is taken for simplicity. This magnetic field is associated with the current

$$\mathbf{j} = \frac{1}{\mu_0}\nabla\times\mathbf{B} = \begin{cases}\mathbf{0} & (\pm y > l_y),\\ (\mu_0 l_x)^{-1}B_0\hat{\mathbf{z}} & (|y| \leqslant l_y).\end{cases} \tag{14}$$

Sharp peaks in the frequency-dependent Kubo conductivity correspond to regular orbits in the given magnetic field and these are analyzed first. Regular orbits in the two-dimensional null are those with a constant adiabatic invariant μ (or magnetic moment) throughout the entire simulation. They are typically the orbits far from the magnetic null. Two motions characterize these orbits, the first being the bounce motion around the hyperbolic field lines of $\mathbf{B}$ [32], which are given by

$$x = \sqrt{y^2 + C^2}$$

outside the l_y region, where C is a constant and $l_y = 0$. Field lines in the region $|y| < l_y$ are simply straight lines that travel from $-l_y$ to l_y with constant x. As a particle travels along a field line, it experiences the mirror force

$$\mathbf{F} = -\mu\nabla B = -\frac{\mu B_0}{l_x}\frac{x\hat{\mathbf{x}} + y\hat{\mathbf{y}}}{\sqrt{x^2+y^2}}, \tag{15}$$

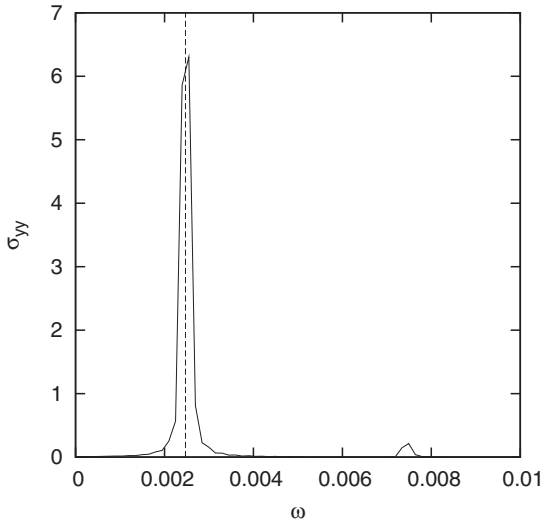

FIG. 1. Conductivity for a typical regular orbit for the two-dimensional magnetic null. Dashed line denotes the theoretical location of the conductivity peak.

where $B_0 = |\mathbf{B}_0|$ is the magnitude of the unit magnetic field. In order to simplify the bounce frequency calculation we set $l_y = 0$. Far along the field lines, the mirror force causes particles to move back toward the null in parabolic orbits. This results in a bounce motion with period and frequency

$$T_B = \frac{2\pi}{\omega_B} = 4\int_0^{y_m} \frac{ds}{v_\parallel} = \frac{4}{v_0}\int_0^{y_m} \frac{\sqrt{2y^2+C^2}}{\sqrt{y^2+C^2}\sqrt{1-\sin^2\theta_0 \frac{\sqrt{2y^2+C^2}}{\sqrt{y_0^2+C^2}}}}dy, \tag{16}$$

where ds is an element of arc length along a field line, y_m is the mirroring point with $v_\parallel = 0$, and θ_0 is the initial pitch angle of the particle. For orbits that pass through the region $|y| < l_y$, an extra term $4l_y/v_{\parallel 0}$ is added, where $v_{\parallel 0}$ is the parallel velocity within the region proper. To test Eq. (16), we use a particle with initial conditions $v_0 = 0.086$, $l_y = 1$, $C = 10$, $\sin\theta_0 = 0.581$, and $y_0 = 0$. This gives $y_m \approx 19.7$ and $\omega_B/2\pi = 3.94 \times 10^{-4}$, which should lead to a sharp peak at $\omega_B = 2.47 \times 10^{-3}$ in the $\sigma_{yy}(\omega)$ conductivity and a sharp peak at $\omega = 2\omega_B$ in the $\sigma_{xx}(\omega)$ conductivity. This agrees with simulation results to within 10% error and the result for $\sigma_{yy}(\omega)$ is presented in Fig. 1.

The second motion that characterizes regular orbits in this magnetic geometry is the ∇B drift,

$$\frac{\mu}{q}\frac{\mathbf{B}\times\nabla B}{B^2} = \begin{cases} \frac{\mu B_0^3}{qB^3 l_x^3}[(y \mp l_y)^2 - x^2]\hat{\mathbf{z}} & (\pm y > l_y), \\ \mu q^{-1} x^{-1}\hat{\mathbf{z}} & (|y| \leqslant l_y), \end{cases} \tag{17}$$

This results in a δ-function peak in the dc ($\omega = 0$) component of the σ_{zz} conductivity. Since $\mathbf{v}_{\nabla B}$ is inversely proportional to the xy coordinates at large distances from the magnetic neutral point, the z-drift velocity is negligible for regular orbits. Apart from the two motions mentioned above, peaks are also expected around the cyclotron frequency (defined using a mean B-field value due to magnetic inhomogeneity) for all diagonal components of the conductivity tensor, corresponding to cyclotron-resonant dissipation. For regular orbits the particles stay in the vicinity of the magnetic null and the cyclotron frequency varies within a small range, resulting in a sharp peak. Conversely, chaotic orbits may have orbits that travel much further away from the null region and the frequency can vary by about an order of magnitude. This produces a broadened cyclotron frequency peak in the frequency-dependent conductivity.

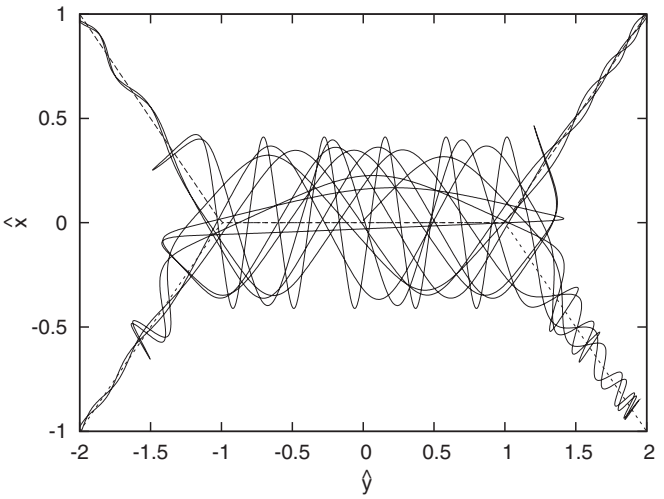

FIG. 2. Typical particle orbit (solid line) in the Y-shaped magnetic field (dotted line) with $l_x = l_y$ and $v_s = 0.05 v_A$.

In Fig. 2 typical orbit for a particle near the chaos region is displayed. Particles that leave the chaos region eventually return due to the mirror force along the field lines. As the mirror force on the particle is directly proportional to the magnetic moment μ, the bounce times may vary considerably as the value of μ will not be conserved once the particle re-enters the chaos region. The violation of the invariance of μ is the signature of these chaotic orbits. The conductivity tensor components for these trajectories contain a spectrum of frequencies that vary depending on the initial conditions and thus reflects the sensitivity of chaotic motion.

Figure 3 illustrates the results of determining the chaos region using the maximal Lyapunov exponent for the $l_x = l_y = 1$

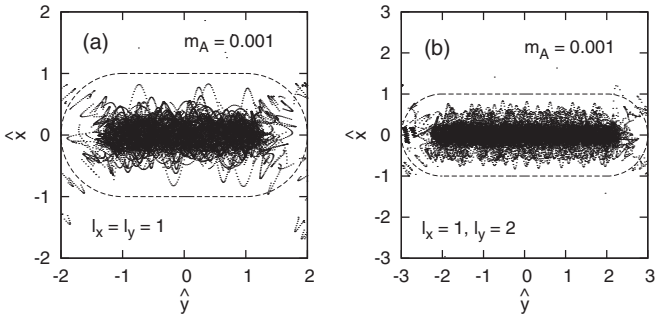

FIG. 3. Chaotic particle trajectories which define the chaos region for the two-dimensional null with $m_A = 0.001$, $l_x = 1$, $l_y = 2$ (a) and $l_y = 1$ (b). Dashed lines indicate the zone of chaos defined in Ref. [18].

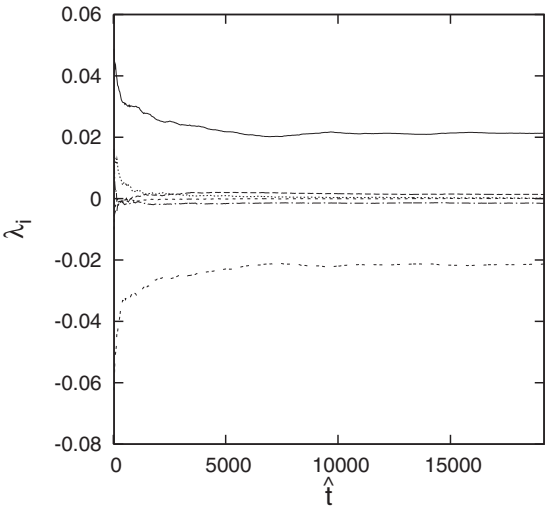

FIG. 4. Typical evolution of the Lyapunov spectrum containing six exponents for an average of 10 particles.

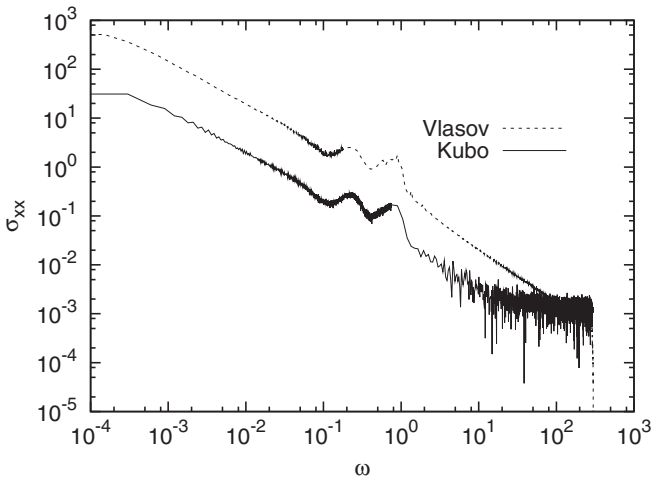

FIG. 5. Comparison between Kubo and Vlasov conductivities computed for the 2D magnetic null. The Vlasov data set has been multiplied by 10 for clarity.

null system as shown in Fig. 3(a) and the $l_x = 1, l_y = 2$ null system given in Fig. 3(b). These were computed by tracking the trajectories of 100 particles over 2×10^6 time steps using a time-step value $\Delta\hat{t} = 0.01$. These results agree with the chaos region defined in Numata and Yoshida [18] that is best described as a stadium-shaped domain; a rectangle centered around the origin with major length $2l_y$ on the y axis, minor length l_x on the x axis, and two half-circles of radius l_x on either side.

The typical evolution of the Lyapunov spectrum for an average of 10 particles over two million time steps is displayed in Fig. 4. All six exponents converge to a definite value for large t, with $\lambda_i = -\lambda_{6-i}$, $i = 1,2,3$. From the computation of the Lyapunov spectrum, averaged over 100 particles, we obtain three positive Lyapunov exponents with the following values: $\lambda_1 \approx 0.02$, $\lambda_2 \approx 0.001$, and $\lambda_3 = 0$, thus indicating chaotic motion.

To test the ergodicity of the system, both Eqs. (3) and (4) were computed and compared. Conductivity computations using Eq. (4) were carried out using an ensemble of 30 000 particles over 2^{21} time steps. The time-step number in base 2 optimizes the computation of the fast Fourier transform (FFT) and is large enough to ensure resolution of the regular and chaotic motion. Particles were initially spread uniformly throughout the chaos region. For the computation of Eq. (3) an initial particle distribution more representative of the entire phase space was needed. This was achieved by taking the Maxwellian particle distribution of five million particles uniformly spread throughout the chaos region and evolving it over 200 000 simulation steps. This created a distribution with particles both inside and outside of the chaos region. The results of these simulations are shown in Fig. 5 and confirmed the ergodicity of the two-dimensional system.

In addition to verifying the ergodicity assumption, the time-averaged Lagrangian velocity autocorrelation was computed in order to check for long-range correlations and anomalous statistics. From the temporal behavior of the velocity autocorrelation presented in Fig. 6 we find that while particles stay in the chaos region their Lagrangian-velocity autocorrelations experience power-law decay with exponents of ~ -0.1. Once particles begin leaving the chaos region, they experience magnetic moment mixing and the decay becomes exponential. However, as integration time is increased the region over which the power law holds similarly increases, reflecting the fact that particles continuously re-enter the chaos region. If this trend holds for arbitrarily long simulation time, then the dc component of the Kubo conductivity tensor may not converge.

For further conductivity calculations the Vlasov conductivity was chosen over the Kubo conductivity since it has the advantage of generating a greater number of correlations in a smaller amount of time. Three cases of initial positions were used where particles are initially placed at specific points in the

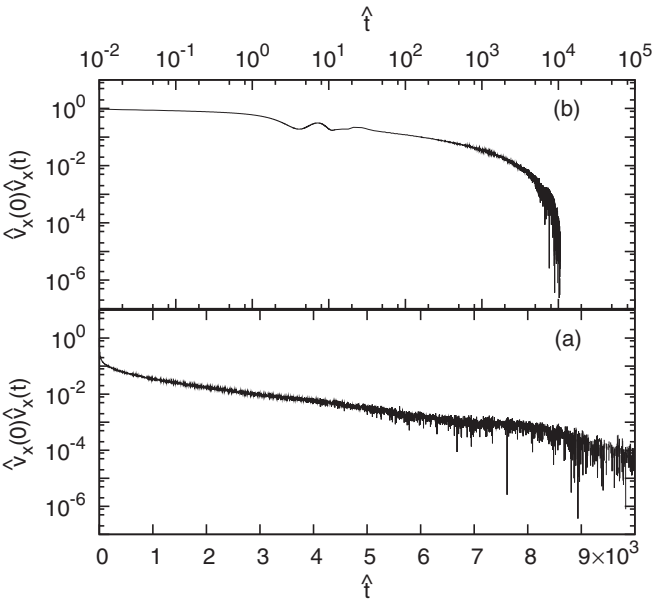

FIG. 6. Lagrangian velocity autocorrelation in the x direction for the 2D magnetic null on a lin-log scale (a) and a log-log scale (b).

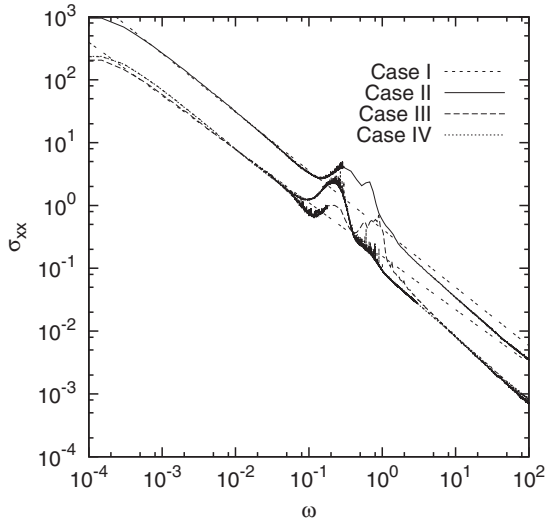

FIG. 7. The conductivity tensor component $\sigma_{xx}(\omega)$. ω and σ_{xx} are in normalized units. Case IV follows the curve of Case I. Power-law fits are shown for Cases III and IV.

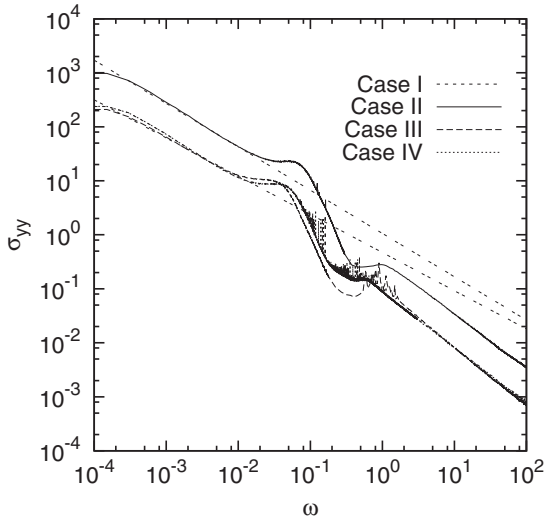

FIG. 8. The conductivity tensor component $\sigma_{yy}(\omega)$. ω and σ_{yy} are in normalized units. Case IV follows the curve of Case I. Power-law fits are shown for Cases III and IV.

chaos region. These positions are $\hat{\mathbf{x}} = (0,0,0),(0,0.5,0)$, and $(0.5,0.5,0)$ denoted by Cases I, II, and III, respectively. Case IV denotes the initial particle ensemble distributed uniformly over the chaos region. All cases were run five times with a different random seed to provide statistics for error analysis. Care must be taken to determine which points in the frequency range represent sufficiently sampled frequencies. A range of frequencies, defined by a minimum and a maximum frequency, can be determined by both the time step and the maximum integration time. The maximum frequency is given by the Nyquist frequency $\omega_{\max} = \pi/\Delta t \approx 300$, while the minimum frequency is given by $\omega_{\min} \approx \pi/N\Delta t = 2 \times 10^{-4}$. In practice, frequencies that fall within a factor of 4 of these cutoffs are also considered to be undersampled. These simulations focus on the case where $l_x = l_y = 1$.

Figure 7 shows the conductivity tensor component $\sigma_{xx}(\omega)$ on a log-log scale in normalized units using one run for each case. The curve for frequencies below the cyclotron frequency $\omega_c \approx 1$ converges to a power law with a unique exponent for all cases and additional peaks appear in the cyclotron frequency range, $0.1 < \omega_c < 5$. The location of these peaks change depending on the initial position of the particles. Power laws of the form $a\omega^b$ are used to fit the conductivity curves in all cases, where a and b are parameters. These functions are fitted using the method of nonlinear least squares [33]. The range over which fitting is performed is determined by running the simulation for varying time intervals and comparing how the curves converge to the power law. In general, the parameter a is of order 10^{-4}, while the exponent b generally falls within the range $-1 < b < -0.5$. Case II exhibits a prefactor (a) that differs from that of the other cases.

Figures 8 and 9 display the conductivity tensor components $\sigma_{yy}(\omega)$ and $\sigma_{zz}(\omega)$, respectively. As with $\sigma_{xx}(\omega)$, simulations show the curve for frequencies below the cyclotron frequency converge to a power law, with additional peaks appearing in the cyclotron frequency range. In all cases, $\sigma_{zz}(\omega)$ displays a jaggedness for small frequencies $\omega \ll \omega_c$. This is characteristic of a numeric δ function $\hat{v}_z^2\delta(\omega)$, where $\hat{v}_z^2$ is the average squared velocity in the z direction. This δ function is a consequence of taking the Fourier transform of a constant function (the average velocity of a single particle in the z direction). Nondiagonal components of the conductivity tensor $\sigma_{\mu\nu}$ are characterized by a noise for small values of ω which eventually disappears for larger frequency values. Since all values on these curves are smaller than their calculated errors, the off-diagonal elements of the conductivity tensor are considered to be zero. The parameters for all power laws $\sigma_{\mu\nu}(\omega) = a_{\mu\nu}\omega^{b_{\mu\nu}}$ are tabulated in Table I. Power-law fits for Cases III and IV are plotted in Figs. 7–9 for illustrative purposes.

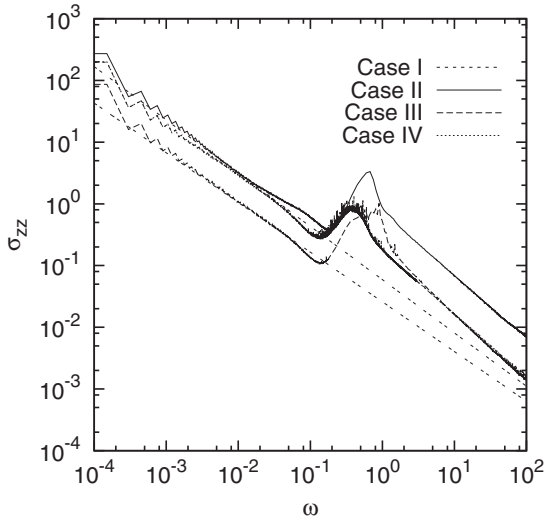

FIG. 9. The conductivity tensor component $\hat{\sigma}_{zz}(\hat{\omega})$. Case IV follows the curve of Case I. Power-law fits are shown for Cases III and IV.

TABLE I. Parameters for the diagonal component power laws of the conductivity tensor in reduced units.

	Case I	Case II
a_{xx}	$(1.126 \pm 0.005) \times 10^{-1}$	$(1.143 \pm 0.08) \times 10^{-1}$
b_{xx}	$(-9.233 \pm 0.004) \times 10^{-1}$	$(-9.208 \pm 0.0013) \times 10^{-1}$
a_{yy}	$(3.16 \pm 0.03) \times 10^{-1}$	$(3.22 \pm 0.05) \times 10^{-1}$
b_{yy}	$(-7.794 \pm 0.014) \times 10^{-1}$	$(-7.77 \pm 0.02) \times 10^{-1}$
a_{zz}	$(1.000 \pm 0.008) \times 10^{-1}$	$(1.013 \pm 0.010) \times 10^{-1}$
b_{zz}	$(-7.370 \pm 0.013) \times 10^{-1}$	$(-7.357 \pm 0.0012) \times 10^{-1}$
	Case III	Case IV
a_{xx}	$(4.23 \pm 0.08) \times 10^{-1}$	$(1.56 \pm 0.03) \times 10^{-1}$
b_{xx}	$(-9.293 \pm 0.004) \times 10^{-1}$	$(-8.51 \pm 0.03) \times 10^{-1}$
a_{yy}	$(1.060 \pm 0.015) \times 10^{-1}$	$(4.7 \pm 0.2) \times 10^{-1}$
b_{yy}	$(-8.02 \pm 0.02) \times 10^{-1}$	$(-7.07 \pm 0.06) \times 10^{-1}$
a_{zz}	$(5.91 \pm 0.09) \times 10^{-2}$	$(2.58 \pm 0.03) \times 10^{-2}$
b_{zz}	$(-8.63 \pm 0.03) \times 10^{-1}$	$(-8.051 \pm 0.0008) \times 10^{-1}$

IV. 3D MAGNETIC NULL MODEL AND CONDUCTIVITY

The most general form of a linear magnetic field around a three-dimensional neutral point at the origin can be described using the form proposed in Ref. [27],

$$\mathbf{B} = \mathbf{M} \cdot \mathbf{r},$$

where $\mathbf{r}$ is the position vector and $\mathbf{M}$ is a 3×3 matrix of the form

$$\mathbf{M} = \begin{bmatrix} 1 & \frac{1}{2}(q - j_\parallel) & 0 \\ \frac{1}{2}(q + j_\parallel) & p & 0 \\ 0 & j_\perp & -(p+1) \end{bmatrix}.$$

Here p and q are potential parameters and $j_\parallel$ and $j_\perp$ are the current parallel and perpendicular to the spine, respectively. In this model, the spine is set along the z axis. We only consider the potential null cases in this paper, therefore we set $j_\perp = j_\parallel = q = 0$, where a rotation of the matrix $\mathbf{M}$ has been performed to eliminate q. This results in the magnetic field

$$\mathbf{B} = [x, py, -(p+1)z]. \tag{18}$$

This potential magnetic null has the fan axis in the xy plane and a spine along the z axis. p must be greater than zero to ensure that the spine remains on the z axis. It is useful to note that when $p > 1$, the magnetic null is identical to the case p^{-1} where the x and y axes have been interchanged, therefore it is only necessary to study the cases where $0 \leqslant p \leqslant 1$. When $p = 0$, the three-dimensional neutral point devolves into a two-dimensional null line lying on the y axis. The case $p = \infty$ is identical to the $p = 0$, with the null line now lying on the x axis. Field lines for the potential nulls are easily solved and can be expressed as

$$y = c_1 x^p, \quad z = c_2 x^{-(1+p)}, \tag{19}$$

where c_1 and c_2 are constants. The element of arc length along a field line is then

$$\begin{aligned} ds^2 &= dx^2 + dy^2 + dz^2 \\ &= dx^2\left[1 + c_1^2 p^2 x^{2(p-1)} + c_2^2 (1+p)^2 x^{-2(2+p)}\right]. \end{aligned} \tag{20}$$

As with the two-dimensional null case, regular orbits of the three-dimensional null are those for which the adiabatic invariant μ is conserved. Typically these orbits occur at great distances away from the magnetic null. Regular dynamics for the three-dimensional potential null ($j_\perp = j_\parallel = 0$, $p \neq 0$) is characterized by two periodic motions around the null point, a bounce motion which oscillates between the spine and the fan plane and a periodic ∇B motion that oscillates around the spine above the fan plane. The bounce motion can be calculated in a procedure similar to the two-dimensional case by integrating an element of arc length of the field line over the parallel velocity at that point, giving the bounce frequency

$$\frac{2\pi}{\omega_B} = 2\int_{x_1}^{x_2} \frac{ds}{v_\parallel} = \frac{2}{v}\int_{x_1}^{x_2} \frac{\sqrt{1 + c_1^2 p^2 x^{2(p-1)} + c_2^2 (1+p)^2 x^{-2(2+p)}}}{\sqrt{1 - \sin^2\theta_0 B_0^{-1}\sqrt{x^2 + c_1^2 p^2 x^{2p} + c_2^2 (p+1)^2 x^{-2(p+1)}}}} dx, \tag{21}$$

where B_0 is the initial magnetic field and x_1, x_2 are the mirror points.

The precession frequency ω_{pre} can also be calculated from the average azimuthal velocity v_θ around the z axis caused by the grad-B drift, as well as the curvature drift. Here we consider the potential null case. The combined grad-B and curvature drift is

$$\begin{aligned} \mathbf{v}_{\mathbf{R}+\nabla B} &= \frac{m}{q}\left(v_\parallel^2 + \frac{1}{2}v_\perp^2\right)\frac{\mathbf{R}_c \times \mathbf{B}}{R_c^2 B^2} \\ &= \frac{m v^2}{2q}\left(2 - \sin^2\theta_0 B_0^{-1} B\right)\frac{\mathbf{R}_c \times \mathbf{B}}{R_c^2 B^2}, \end{aligned} \tag{22}$$

where $\sin\theta_0$ is the particle's initial pitch angle, $B = |\mathbf{B}|$, and $\mathbf{R}_c$ is the radius of curvature vector with magnitude

$$R_c = \frac{\left[1 + \left(\frac{df(x)}{dx}\right)^2\right]^{3/2}}{\left|\frac{d^2 f(x)}{dx^2}\right|} \tag{23}$$

and lies in the direction of curvature. Here $f(x)$ is the function that defines a field line in terms of the variable x. The precession frequency ω_{pre} is calculated using

$$\omega_{\text{pre}} = \langle v_\theta \rangle = \left(\frac{1}{s_2 - s_1}\int_{s_1}^{s_2} v_\theta ds\right), \tag{24}$$

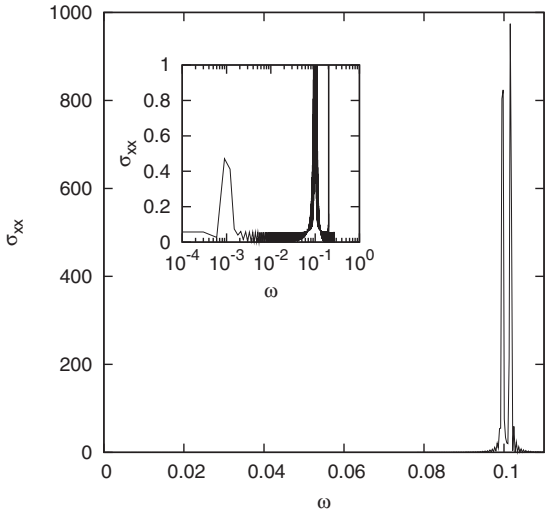

FIG. 10. Conductivity for a typical regular orbit for the three-dimensional magnetic null. Inset illustrated the precession peak around the spine axis.

where s_1 and s_2 are the mirror points of the given field line and

$$v_\theta = \frac{\mathbf{v}_{\mathbf{R}+\nabla B}}{\sqrt{x^2+y^2}}.$$

If the simplest case is considered, using a particle confined to the xz plane with $p = 1$, this becomes

$$\begin{aligned}\omega_{\rm pre} &= \frac{1}{x_2-x_1}\int_{x_1}^{x_2}\frac{m}{q}\left(v^2-\frac{1}{2}v_\perp^2\right)\frac{6c_2x^{-5}}{\left(1+4c_2^2x^{-6}\right)^{3/2}}dx \\ &= \frac{1}{x_2-x_1}\int_{x_2}^{x_1}\frac{mv^2}{2qB}\left(2-\sin_0^2\theta B_0^{-1}B\right) \\ &\quad\times\frac{6c_2x^{-5}}{\left(1+4c_2^2x^{-6}\right)^{3/2}}dx, \qquad (25)\end{aligned}$$

where $B=\sqrt{x^2+4c_2^2x^{-4}}$.

To verify the above equations, solutions are obtained using a particle with initial parameters $c_1 = 0$, $c_2 = 421.9$, $B_0 = 16.8$, $\sin\theta_0 = 0.679$, and $v = 3.055$. From this simulation, the mirror points are determined to be $x_1 = 4.95$ and $x_2 = 35.6$, which gives a bounce frequency $\omega_B = 0.101$ and precession frequency $\omega_{\rm pre} = 1.34\times10^{-3}$, in normalized units. Since these two motions form a product of cosines the bounce frequency peak actually splits into two peaks with upper and lower frequencies $\omega_{B,\pm} = \omega_B \pm \omega_{\rm pre}$. The bounce frequency agrees with simulation results to within an error of approximately 5%, while Eq. (25) somewhat overestimates the simulation results by approximately 30% . The conductivity frequency spectrum results are shown in Fig. 10.

Figure 11 illustrates the chaos region for potential nulls for p values 1,0.75,0.5,0.25, and 0 calculated using the maximal Lyapunov exponent. As in Sec. III, these plots were generated by tracking the trajectories of 100 particles over 2×10^6 steps using time step $\Delta\hat{t} = 0.01$. The initial velocities of the particles are drawn from a Maxwellian distribution with normalized thermal velocity $\hat{v}_T = 0.05$ and placed uniformly over a prolate ellipsoid that has unit semiminor axes and a

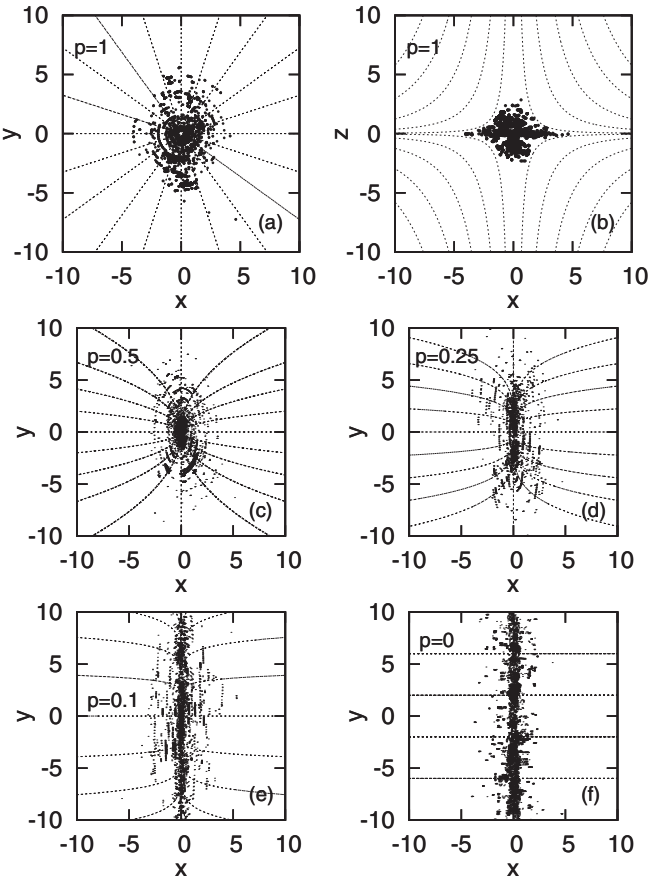

FIG. 11. Chaotic particle trajectories for systems with varying values of p, $q = j_\parallel = j_\perp = 0$. Dashed lines indicate magnetic field lines. Panels (a) and (b) are the x-y and x-z projections for $p = 1$, respectively. Panels (c)–(f) show the elongation of the chaos region in the y direction for $p = 0.75,0.5,0.25$, and 0, respectively.

semimajor axis equal to $1/p$ for the results in Figs. 11(a)–11(e) and over a uniform unit disk in Fig. 11(f). Figures 11(a) and 11(b) show the x-y and x-z projections for the $p = 1$ case, respectively. The eigenvectors for potential nulls are the x, y, and z unit vectors, where the z unit vector corresponds to the spine and the x, y unit vectors correspond to the major and minor axes of the fan, respectively. The chaos region for this case is best described as a sphere of unit radius, which reflects the azimuthal symmetry of the $p = 1$ system. This symmetry is broken for other values of p, as can be seen in Figs. 11(c)–11(f). For systems having $0 < p < 1$ the sphere becomes an ellipsoid with a unit minor radius and a major radius equal to p^{-1}. Here the minor axis of the ellipsoid lies along the major axis of the fan, while the major axis of the ellipsoid lies along the minor axis of the fan. The x-z projections of these systems are similar to that of the $p = 1$ case and therefore are not shown in this diagram. For $p = 0$ the chaos region is an infinitely long cylinder of unit radius since the y direction is spatially symmetric. The Lyapunov spectra for all systems were computed using 2^{21} steps, averaged over 100 particles. The first (maximal) Lyapunov exponents are of the order 10^{-2} while the second exponents are approximately 10^{-4}. The two-dimensional $p = 0$ system has the largest MLE, while the

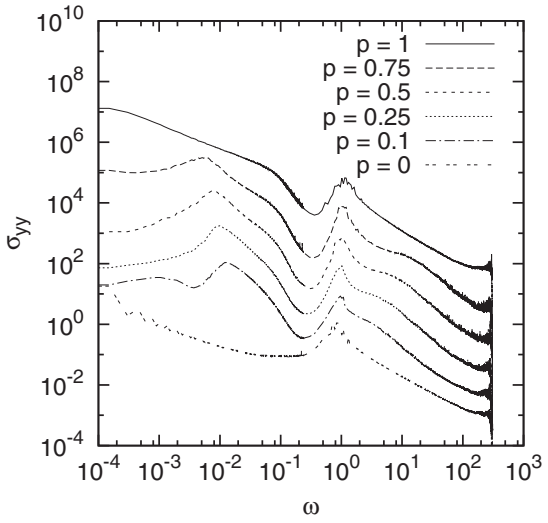

FIG. 12. Normalized conductivity tensor component $\sigma_{yy}(\omega)$ for cases dealing with the potential magnetic null. Data sets for $p > 0$ have been multiplied by increasing powers of 10 for clarity.

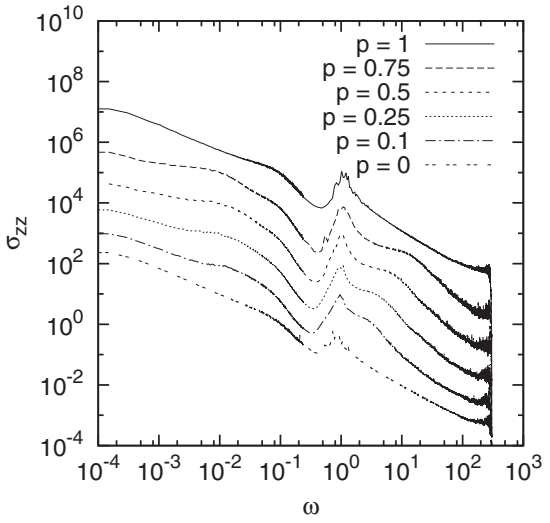

FIG. 14. Normalized conductivity tensor component $\sigma_{zz}(\omega)$ for cases dealing with the potential magnetic null. Data sets for $p > 0$ have been multiplied by increasing powers of 10 for clarity.

$p = 0.5$ system has the largest MLE for the three-dimensional nulls.

To test the ergodicity of the three-dimensional system, Eqs. (3) and (4) were computed for the $p = 1$ system and verified to be the same. Initial particle distributions were prepared using the same procedure described in Sec. III. The $p = 0$ is also ergodic as it is topologically similar to the two-dimensional magnetic null system described in the previous section. It is assumed that the other cases studied here, which are topologically similar to the $p = 1$ case, are also ergodic. For the remainder of the paper, Eq. (4) is used to compute the conductivity.

Since the y component of the magnetic field is the most topologically dependent on the parameter p, the tensor component $\sigma_{yy}(\omega)$ will be considered first. Figure 12 shows the

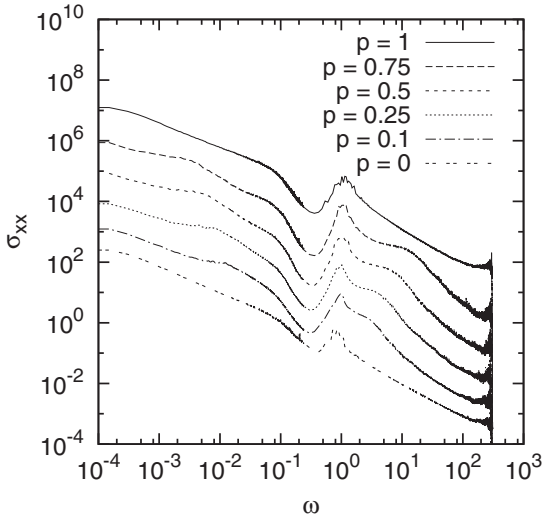

FIG. 13. Normalized conductivity tensor component $\sigma_{xx}(\omega)$ for cases dealing with the potential magnetic null. Data sets for $p > 0$ have been multiplied by increasing powers of 10 for clarity.

yy component of the conductivity tensor for all potential cases. Cyclotron motion produces peaks in all cases for frequencies around unity, with the $p = 1$ case following a clear power law $[\sigma_{\mu\nu}(\omega) = a_{\mu\nu}\omega^{b_{\mu\nu}}]$ for the lower frequencies. In all cases, the conductivity for frequencies above the cyclotron region $\omega > 10$ becomes negligible. The $p = 0$ conductivity below the cyclotron frequency follows a power law with an additional δ function which represents the average squared velocity in the y direction and is of the order 10^{-5}. For intermediate cases where $0 < p < 1$, a distinct peak around $\omega = 10^{-2}$ is seen, with a decrease in conductivity for decreasing ω. As the simulation time is increased, these peaks shift towards smaller

TABLE II. Parameters for the potential null power laws.

p	a_{xx}	b_{yy}
0	0.182 ± 0.002	-0.861 ± 0.002
0.1	0.342 ± 0.004	-0.661 ± 0.003
0.25	0.754 ± 0.008	-0.509 ± 0.004
0.5	0.377 ± 0.006	-0.637 ± 0.003
0.75	0.351 ± 0.06	-0.654 ± 0.003
1	0.173 ± 0.002	-0.774 ± 0.002
p	a_{yy}	b_{yy}
0	$(8.82 \pm 0.05) \times 10^{-3}$	-0.650 ± 0.003
0.1	$(5.98 \pm 0.15) \times 10^{-3}$	-1.810 ± 0.009
0.25	$(5.94 \pm 0.10) \times 10^{-3}$	-1.785 ± 0.005
0.5	$(9.10 \pm 0.11) \times 10^{-3}$	-1.654 ± 0.003
0.75	$(1.93 \pm 0.10) \times 10^{-2}$	-1.423 ± 0.003
1	0.173 ± 0.005	-0.775 ± 0.002
p	a_{zz}	b_{zz}
0	0.181 ± 0.003	-0.861 ± 0.002
0.1	0.270 ± 0.013	-0.689 ± 0.009
0.25	0.754 ± 0.007	-0.509 ± 0.002
0.5	0.876 ± 0.004	-0.459 ± 0.002
0.75	0.829 ± 0.011	-0.479 ± 0.03
1	0.131 ± 0.003	-0.808 ± 0.005

ω and decrease in width and the conductivity curves appear to converge on a power law. Assuming this trend holds for arbitrarily long simulation time, the power laws are computed using the points taken from the frequency region between the peak in question and the cyclotron frequency peak.

Figures 13 and 14 show the conductivity tensor components $\sigma_{xx}(\omega)$ and $\sigma_{zz}(\omega)$ on a log-log scale in normalized units using one run for each case, respectively. As with the $\sigma_{yy}(\omega)$ case, as simulation time is increased the conductivity components tend to converge to power laws below the cyclotron frequency $\omega_c \sim 1$. For $\sigma_{xx}(\omega)$, cases $p = 0$ and $p = 1$ follow an overall similar shape, with the rest of the cases varying slightly. These differences become more pronounced for the $\sigma_{zz}(\omega)$ component. As with the two-dimensional case, off-diagonal tensor components are negligible when compared to their respective errors and are thus not considered here. Power-law fits for all three-dimensional cases are tabulated in Table II.

V. DISCUSSION AND SUMMARY

Various methods can be used to compute the conductivity for collisionless-type plasmas. In this paper, starting with 2D and 3D magnetic null configurations, we have compared the local dc conductivity ($\omega = 0$) obtained from the mean-drift method with the ac conductivity using the Kubo formalism. At a microscopic level, both of these conductivities can be related to the lifetime of the particles in the null region.

Speiser [10] defines a general conductivity of the form

$$\sigma_s = \frac{ne^2}{m}\tau_s, \tag{26}$$

where τ_s is some effective collision time of the system. He demonstrates three different effective collision times, one representing collisional conductivity while the other two represent collisionless conductivities. The first collisionless conductivity is based on the finite average lifetime of particles inside the current sheet layer, where particles typically diffuse. Here, the particles are freely accelerated by an applied electric field. Once these particles leave the current sheet layer, they resume regular motion and the acceleration ceases. The second collisionless conductivity defined by Speiser is related to the particle gyromotion and the $\mathbf{E} \times \mathbf{B}$ drift which leads to an effective collision time $\tau_g = m/qB_\perp = \omega_c^{-1}$. This conductivity is an off-diagonal element of the complete conductivity tensor.

The mean-drift method can be related to the conductivity formula in Eq. (26). For the particular case of the 2D magnetic null, Numata and Yoshida [18] found that, in normalized units, the particle staying time is equal to the reciprocal of the Alfvén Mach number (m_{A}^{-1}, where $m_A \equiv E_0/B_0V_A$), provided that $l_y/l_x \lesssim 10$. This particle staying time becomes the effective collision time in Eq. (26) and is not unlike the first collisionless conductivity mentioned by Speiser. For chaotic motion, this particle staying time must be sufficiently large compared to the MLE, which requires that $m_A \lesssim 10^{-2}$.

Since the magnetic field for the two-dimensional magnetic null is self-consistent, an approximate conductivity can be derived by combining Ohm's law with Ampère's law,

$$\sigma = \frac{\nabla \times \mathbf{B}}{\mu_0 \mathbf{E}}, \tag{27}$$

which in normalized units gives

$$\hat{\sigma} = \begin{cases} 0 & (\pm y > l_y), \\ m_A^{-1} & (|y| \leqslant l_y), \end{cases} \tag{28}$$

where m_A is the Alfvén Mach number. The computed conductivity of the system depends on how much time the particles spend within the range $|y| \leqslant l_y$. Self-consistent electric fields become much more complicated in the three-dimensional system (see Ref. [32]) and we do not consider these effects in this work.

The two main contributions to the ac conductivity are cyclotron motion, which manifests itself as peaks around the cyclotron region ($\omega \sim 1$) and correlated bounce motion from particles leaving from and returning to the magnetic null region. For linear magnetic fields at distances far away from the magnetic null, the mirror force is constant and is proportional to the first adiabatic invariant μ, resulting in parabolic trajectories along magnetic field lines. The violation of the invariance of μ around the magnetic null causes bounce frequency mixing which results in a broad power spectrum in the conductivity. Conversely, regular orbits drawn from a Maxwellian result in sharp peaks for both cyclotron and bounce motion. This bounce frequency contribution is not captured in the Speiser/Numata-Yoshida formulation of the conductivity. It is important to compare the magnitude of the ac conductivity to the dc conductivities mentioned above. For the two-dimensional model, conductivities around the cyclotron frequency region $\omega \sim 1$ are of the order of unity, $\hat{\sigma}_{\mathrm{ac}} \sim 1$, which is an order of magnitude smaller than the dc conductivity. The dissipation, while negligible for small frequencies and dc values, can play a significant role when the electric field frequency is close to the cyclotron frequency. The diagonal elements of the Kubo conductivity tensor follow power laws for electric field frequencies below the cyclotron frequency. This reflects the fact that the Fourier transform of a power law t^α with exponent $-1 < \alpha < 0$ is also a power law with exponent $-(1 + \alpha)$. The velocity autocorrelations of chaotic orbits usually obey these types of power laws. This results in diverging values for the dc conductivity, though the divergence in itself is not a problem as an infinite conductivity simply implies zero resistivity.

It is clear that different formulations of the conductivity give different results. The Kubo conductivity may not be well suited for calculating the dc conductivity on systems where particles are known to escape quickly. The time spent outside the chaos region may also be problematic, as the bounce motion of a particle can be greatly affected by the drift velocity introduced by an applied electric field. In these situations the particle can leave the chaos region and not return. For this, a finite-lifetime model may be more appropriate. However, correlated motions over the entire region inside and outside the zone of chaos can become important for ac electric fields with frequencies on the order of the cyclotron frequency. The Kubo conductivity is able to properly account for these motions, which makes it a powerful tool for computing ac conductivities.

Interesting features arose from the Kubo conductivity when applied to three-dimensional magnetic nulls. As with the two-dimensional cases, the conductivities are generally well described by power laws. For the potential systems,

the region around $\omega \sim 0.2$ shows a noticeable decrease in conductivity. This inverted peak can be considered the region that lies between the bounce frequency mixing and the cyclotron motion regime. As with the two-dimensional cases, the conductivity is of order unity when the ac frequency is around the cyclotron region. Throughout the entire range of frequencies, the magnitude of the potential null conductivities are similar to that of the two-dimensional cases, though the spectra differ substantially. This can be attributed to the total area underneath the conductivity curve, given by Eq. (7). Once again, the Kubo conductivity becomes significant when dealing with ac perturbations when the frequency is around the cyclotron region.

Simulations revealed that the yy component of the potential conductivity tensor was greatly dependent on the value of the parameter p. The regions of chaos for these potential nulls are well defined as an ellipsoid with major radius on the y axis with magnitude equal to p^{-1}. As the symmetry of the magnetic null breaks, so does the symmetry in xx and yy components of the conductivity tensor. However, there appears to be a disconnect between the conductivity curves of the potential null cases $p = 0.1$ and $p = 0$, as well as the cases $p = 1$ and $p = 0.75$. These curves show that even without current, complex behavior can arise from even simple linear potential nulls.

The average dissipation $\langle \mathbf{j} \cdot \mathbf{E} \rangle$ can be estimated, though the Kubo conductivity does not enable direct computation. Here we consider the current as a sum of equilibrium and perturbation values,

$$\mathbf{j} = \mathbf{j}_0 + \delta\mathbf{j} = \mathbf{j}_0 + \sigma\delta\mathbf{E}. \tag{29}$$

For either of the two-dimensional null systems, the average equilibrium current in the z direction is governed by the grad-B drift. However, this drift has opposite directions for either side of the magnetic null line, which results in no average current for the equilibrium system. To calculate the perturbation dissipation D, we assume a periodic electric field,

$$D(\omega) = \langle \mathbf{j} \cdot \mathbf{E}_0 \cos(\omega t) \rangle = \frac{\sum_i \sum_j \sigma_{ij}(\omega) E_{j0} E_{i0}}{2} = \frac{\sum_i \sum_j \rho_{ij}(\omega) j_j j_i}{2}, \tag{30}$$

where $i, j = x, y, z$, which is positive provided the conductivity tensor is also positive, angular brackets denote the average over the entire space and time domain, and $\rho_{ij} = 1/\sigma_{ij}$ is the resistivity. The above formula is valid for systems with both regular and chaotic orbits. For regular systems, cyclotron resonance is experienced only near the peaks around the cyclotron frequency ($\omega \sim \omega_c$) and the bounce frequency ($\omega \sim \omega_B$). For chaotic systems, irreversible dissipation will take place over a broad spectrum of frequencies, with the strongest dissipation occurring around and below the cyclotron frequency ($\omega \leqslant \omega_c$). In order to compute the total dissipation, both the dc and ac conductivities must be taken into account.

To summarize, in this paper we found that while the Kubo conductivity cannot be used to compute the dc conductivity of potential linear magnetic nulls, it can be used to generate a full spectrum of ac conductivities, which can become very important in magnetic null systems found in collisionless plasma environments. In order to properly handle both types of conductivities, the domain of chaos must be determined on a case-by-case basis for specific magnetic systems. The Kubo conductivity is characterized by a power-law behavior with frequency which reflects the decay of correlated motion in chaotic systems. This behavior plays an important role when determining the energy dissipation of the system.

ACKNOWLEDGMENTS

This work was supported by the Natural Science and Engineering Research Council (NSERC) of Canada and D.St.O. thanks NSERC for a Postgraduate Research Scholarship. We also thank Westgrid Canada for providing computational resources for this research.

[1] R. G. Giovanelli, Mon. Not. R. Astron. Soc. **107**, 338 (1947).
[2] F. Hoyle, *Some Recent Researches in Solar Physics* (Cambridge University Press, New York, 1949).
[3] J. W. Dungey, Philos. Mag. Ser. 7 **44**, 725 (1953).
[4] A. Stark, W. Fox, J. Egedal, O. Grulke, and T. Klinger, Phys. Rev. Lett. **95**, 235005 (2005).
[5] H. E. Petschek, in *The Physics of Solar Flares, Proceedings of the AAS-NASA Symposium*, edited by W. N. Hess (National Aeronautics and Space Administration, Washington, DC, 1964), p. 425.
[6] E. R. Priest and T. G. Forbes, J. Geophys. Res. **91**, 5579 (1986).
[7] M. Jardine and E. R. Priest, J. Plasma Phys. **42**, 111 (1989).
[8] R. Kulsrud, Earth Planets Space **53**, 417 (2001).
[9] H. Baty, E. R. Priest, and T. G. Forbes, Phys. Plasmas **16**, 060701 (2009).
[10] T. W. Speiser, Planet Space Sci. **18**, 613 (1970).
[11] R. Kubo, J. Phys. Soc. Jpn. **12**, 570 (1957).
[12] W. Horton, C. Liu, B. Burns, and T. Tajima, Phys. Fluids. B **3**, 2192 (1991).
[13] I. J. D. Craig and A. N. McClymont, AstroPhys. J. **371**, L41 (1991).
[14] L. Fletcher and P. Petkaki, Solar Phys. **172**, 267 (1997).
[15] Y. Litvinenko, Solar Phys. **216**, 189 (2003).
[16] P. Petkaki and A. Mackinnon, Astron. Astrophys. **472**, 623 (2007).
[17] R. F. Martin, Jr., J. Geophys. Res. : Space Phys. **91**, 11985 (1986).
[18] R. Numata and Z. Yoshida, Phys. Rev. Lett. **88**, 045003 (2002).
[19] R. Numata and Z. Yoshida, Phys. Rev. E **68**, 016407 (2003).
[20] W. Horton and T. Tajima, Geophys. Res. Let. **17**, 123 (1990).
[21] W. Horton and T. Tajima, J. Geophys. Res. **96**, 15811 (1991).
[22] D. L. Holland and J. Chen, Geophys. Res. Lett. **19**, 1231 (1992).
[23] S. W. H. Cowley, Planet. Space Sci. **26**, 539 (1978).
[24] J. Hernandez, W. Horton, and T. Tajima, J. Geophys. Res. **98**, 5893 (1993).
[25] S. W. H. Cowley, Radio Sci. **8**, 903 (1973).
[26] S. Fukao, M. Ugai, and T. Tsuda, Rep. Ionos. Space Res. Jpn. **29**, 133 (1975).

[27] C. E. Parnell, J. M. Smith, T. Neukirch, and E. R. Priest, Phys. Plasmas **3**, 759 (1996).

[28] C. J. Xiao, X. G. Wang, Z. Y. Pu, H. Zhao, J. X. Wang, Z. W. Ma, S. Y. Fu, M. G. Kivelson, Z. X. Liu, Q. G. Zong, K. H. Glassmeier, A. Balogh, A. Korth, H. Reme, and C. P. Escoubet, Nat. Phys. **2**, 478 (2006).

[29] G. Benettin, L. Galgani, A. Giorgilli, and J.-M. Strelcyn, Meccanica **15**, 9 (1980).

[30] I. Shimada and T. Nagashima, Prog. Theor. Phys. **61**, 1605 (1979).

[31] R. Kubo, Rep. Prog. Phys. **29**, 255 (1966).

[32] E. R. Priest and V. S. Titov, Phil. Trans. R. Soc. Lond. A **354**, 2951 (1996).

[33] W. H. Press, S. Teukolsky, W. Vetterling, and B. Flannery, *Numerical Recipes: The Art of Scientific Computing* (Cambridge University Press, New York, 2007).